PHYSICS

Reconfigurable nanoscale spin-wave directional coupler

Qi Wang,[1] Philipp Pirro,[1] Roman Verba,[2] Andrei Slavin,[3] Burkard Hillebrands,[1] Andrii V. Chumak[1]*

Spin waves, and their quanta magnons, are prospective data carriers in future signal processing systems because Gilbert damping associated with the spin-wave propagation can be made substantially lower than the Joule heat losses in electronic devices. Although individual spin-wave signal processing devices have been successfully developed, the challenging contemporary problem is the formation of two-dimensional planar integrated spin-wave circuits. Using both micromagnetic modeling and analytical theory, we present an effective solution of this problem based on the dipolar interaction between two laterally adjacent nanoscale spin-wave waveguides. The developed device based on this principle can work as a multifunctional and dynamically reconfigurable signal directional coupler performing the functions of a waveguide crossing element, tunable power splitter, frequency separator, or multiplexer. The proposed design of a spin-wave directional coupler can be used both in digital logic circuits intended for spin-wave computing and in analog microwave signal processing devices.

INTRODUCTION

Spin waves (SWs) are orders of magnitude shorter compared to electromagnetic waves of the same frequency, and therefore, the use of SWs allows one to design much smaller nanosized devices for both analog and digital data processing (*1*–*15*). Recently, several novel concepts of magnonic logic and signal processing have been proposed (*2*, *3*, *6*, *16*–*25*), but one of the unsolved problems of the magnonic technology is an effective and controllable connection of separate magnonic signal processing devices into a functioning magnonic circuit (*6*). Unfortunately, a simple X-type crossing (*21*, *26*) has a significant drawback because it acts as an SW re-emitter into all four connected SW channels. Thus, an alternative solution for an SW device connector is necessary.

We propose to use dipolar interaction between magnetized or self-biased, laterally parallel SW waveguides to realize a controlled connection between magnonic conduits. Originally, such an SW coupling has been studied theoretically in a "sandwich-like" vertical structure consisting of two infinite films separated by a gap (*27*, *28*). However, experimental studies of this structure are rather complicated due to the lack of access to the separate layers, which is required for the excitation and detection of propagating SWs. The configuration of a connector based on two laterally adjacent waveguides is well studied in integrated optics because it can be conveniently implemented in applications (*29*). Recently, the dipolar coupling between two externally magnetized millimeter-sized laterally adjacent magnetic stripes has been studied experimentally using Brillouin light scattering spectroscopy by Sadovnikov and colleagues (*30*–*32*). It has been shown that SW coupling efficiency depends on both the geometry of a magnonic waveguides and the characteristics of the interacting SW modes (*30*). Also, a nonlinear regime of the SW waveguide coupling has been experimentally investigated in millimeter-sized waveguides (*31*).

However, to make a directional coupler based on the dipolar interaction between laterally adjacent SW waveguides usable in contemporary magnonic circuits, this device should be substantially more compact (nanometer instead of millimeter in size), should be able to function without permanent bias magnetic field, should have sufficiently low propagation losses (related to both Gilbert damping and waveguide reflections), and should be easily integrable into large magnonic circuits without additional input and output transducers. Also, it is necessary to develop an analytic theory of operation of such a device, which would allow one to easily adjust and optimize the device characteristics for a particular application.

Here, we study dipolar coupling of nanoscale self-biased SW waveguides and propose a practical design of a nanoscale magnonic directional coupler. We do this using the combination of micromagnetic simulations and analytical theory, which we developed for easy optimization of the device characteristics. The proposed directional coupler consists of two bent nanosized and self-biased SW waveguides, where the bent regions are placed laterally close to each other, thus defining a region of the waveguides where the dipolar coupling is taking place. The chosen particular shape of the bent regions ensures a highly efficient (more than 95%) SW transmission that is difficult to achieve on the waveguides of a millimeter-size (*33*) or even micrometer-size (*19*, *21*) scales. Using micromagnetic simulations, we demonstrate that the proposed SW directional coupler can have different functionalities (connector, power divider, frequency separator, multiplexer, etc.) controlled by the external parameters, such as the frequency (wave number) of the propagating SW, length of the "coupling" region of the waveguides, relative orientation of the static magnetizations in the coupled parallel waveguide segments, and the magnitude of the permanent bias magnetic field (which might be used but is not essential). It is also demonstrated that the working parameters and the functionality of the proposed device can be dynamically reconfigured by application of a short (tens of nanoseconds) pulse of an external bias magnetic field.

Operational principle of the directional coupler

In the case when two identical magnetic strip-line SW waveguides are placed sufficiently close to one another (see Fig. 1A), the dipolar coupling between the waveguides leads to a splitting of the lowest width SW mode of a single waveguide into the symmetric ("acoustic") and antisymmetric ("optic") collective modes of the coupled waveguides (see Fig. 1, B and C). Thus, in a system of two dipolarly coupled waveguides, at each frequency, two SW modes (symmetric and antisymmetric, whose profiles are shown in Fig. 1C) with different wave numbers k_s and k_{as} ($\Delta k_x = |k_s - k_{as}|$) will be excited simultaneously. The interference between these two propagating waveguide modes will lead to a periodic transfer of energy from one waveguide to the other (see Fig. 1A), so the energy of an SW excited in one of the waveguides

[1]Fachbereich Physik and Landesforschungszentrum OPTIMAS, Technische Universität Kaiserslautern, Kaiserslautern 67663, Germany. [2]Institute of Magnetism, Kyiv 03680, Ukraine. [3]Department of Physics, Oakland University, Rochester, MI 48309, USA.
*Corresponding author. Email: chumak@physik.uni-kl.de

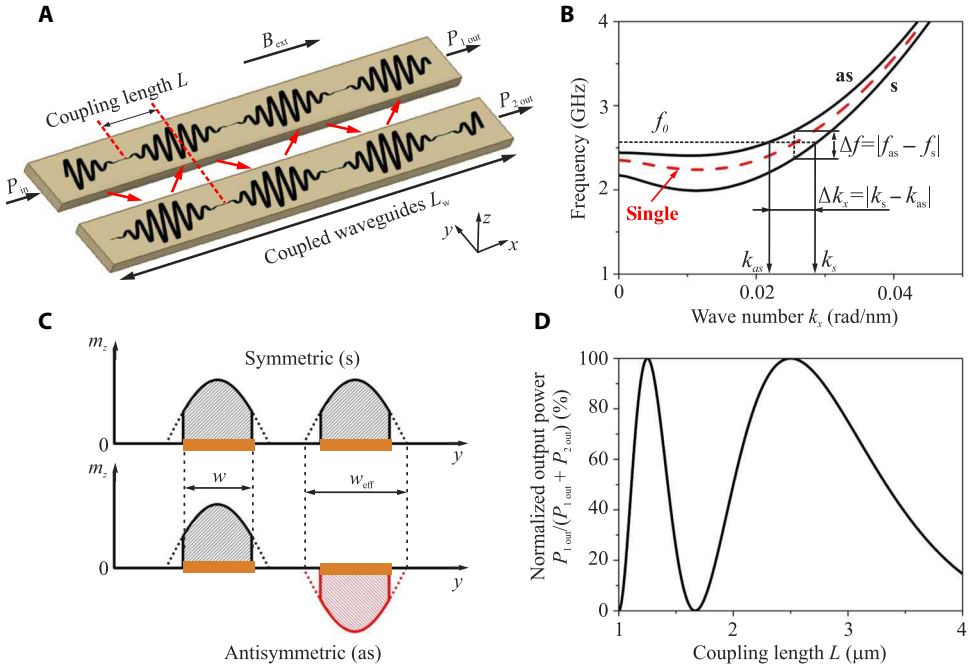

Fig. 1. The operational principle of a directional coupler based on two dipolarly coupled SW waveguides. (**A**) Sketch of two dipolarly coupled SW waveguides. Solid red lines illustrate the periodic energy exchange between the two interacting SW waveguides with a spatial periodicity of 2*L*. (**B**) The red dashed line shows the dispersion characteristic of the lowest SW width mode in an isolated single SW waveguide. Solid black lines show the dispersion curves of the "symmetric" (s) and "antisymmetric" (as) lowest collective SW modes of a pair of dipolarly coupled SW waveguides. (**C**) Spatial profiles of the "symmetric" (s) and "antisymmetric" (as) collective SW modes partially pinned at the waveguide lateral boundaries ($w_{eff} > w$; see the main text). (**D**) Normalized output power of the first waveguide of the directional coupler as a function of the coupling length *L* (varied by varying the spin-wave wave number as will be shown later) for a fixed length of the coupled waveguides $L_w = 5$ μm, external field $B_{ext} = 10$ mT, and vanishing damping in the system.

will be transferred to the other waveguide after propagation over a certain distance that will be defined as the coupling length *L* (*28*)

$$L = \pi/\Delta k_x = \pi/|k_s - k_{as}| \quad (1)$$

Note that, in our case, spins at the lateral boundaries are pinned only partially (*34*, *35*), and therefore, we introduce the "effective width" of the waveguides w_{eff} that can be larger than the nominal waveguide width *w* (see Fig. 1C). This issue is discussed in more detail below.

The difference in the wave numbers Δk_x of the modes of the same frequency is equal to $\Delta k_x = \Delta\omega/(\partial\omega_0/\partial k_x) = \Delta\omega/v_{gr}$, where $\Delta\omega = 2\pi\Delta f$, $\Delta f = |f_{as} - f_s|$ is the frequency separation between the symmetric (f_s) and antisymmetric modes (f_{as}) (see Fig. 1B), and $\omega_0 = 2\pi f_0$, f_0 is the SW frequency. With this last expression, the coupling length can be rewritten as

$$L = v_{gr}/(2\Delta f) \quad (2)$$

where v_{gr} is the SW group velocity in a single isolated waveguide.

The case interesting for applications is the one when an SW is originally excited in only one SW waveguide. The output powers for both waveguides can be expressed as follows (*28*): $P_{1\ out} = P_{in}\cos^2(\pi L_W/(2L))$ for the first waveguide and $P_{2\ out} = P_{in}\sin^2(\pi L_W/(2L))$ for the second one, where L_W is the length of the coupled waveguides as shown in Fig. 1A and P_{in} is the input SW power in the first waveguide. The dependence of the normalized output power of the first waveguide $P_{1\ out}/(P_{1\ out} + P_{2\ out})$ can be expressed as

$$P_{1\ out}/(P_{1\ out} + P_{2\ out}) = \cos^2(\pi L_W/(2L)) \quad (3)$$

This dependence is shown in Fig. 1D as a function of the coupling length *L* for the case when damping is ignored.

Thus, the interplay between the length of the coupled waveguides L_W and the coupling length *L*, which is strongly dependent on several external and internal parameters of the system, allows one to define the ratio between the SW powers at the outputs of two coupled waveguides and, thus, define the functionality of the investigated directional coupler. In particular, we demonstrate below that the functionality of the directional coupler can be changed by varying the geometrical sizes of the waveguides and spacing in between them by changing the SW frequency (wave number) and/or the applied bias magnetic field and changing the relative orientations of static magnetizations of the interacting SW waveguides.

An analytical theory of coupled waveguides

To analytically describe the energy transfer in the system of two coupled waveguides, we first need to find the dispersion relation and the spatial profiles of the SW eigenmodes in them. When two waveguides are coupled, the SW branch existing in an isolated waveguide is split into two collective SW modes. In the simplest case of identical waveguides, these collective modes are symmetric and antisymmetric (see Fig. 1C).

To obtain the dispersion relation and the spatial structure of the collective modes in a general case, one needs to solve the Landau-Lifshitz (LL) equation of magnetization motion

$$\frac{d\mathbf{M}}{dt} = -|\gamma|\mathbf{M} \times \mathbf{B}_{\text{eff}} \tag{4}$$

in the linear approximation and neglecting the damping term. Here, $\mathbf{M}$ is the magnetization vector, $\mathbf{B}_{\text{eff}}$ is the effective field (which includes exchange, external, and demagnetization fields), and γ is the gyromagnetic ratio. In the following, we assume that the dynamic component of the magnetization is constant across the waveguide thickness (uniform thickness profile) that is a good approximation for waveguide thicknesses of the order of hundred nanometers and smaller. Within this approximation, the SW spectra can be calculated using the formalism developed by Verba and colleagues (*36*, *37*) for the case of coupled magnetic nanodots but with the difference that SW propagation along the nanowire waveguides should be taken into account.

We consider two identical SW waveguides and identical SW modes propagating along these waveguides in the x direction. Then, the magnetization in a waveguide can be written as $\mathbf{M}(\mathbf{r}, t) = M_s(\boldsymbol{\mu} + \mathbf{m}(y)\exp(i(kx + \omega_k t)))$, where M_s is the saturation magnetization, $\boldsymbol{\mu}$ is the unit vector in the direction of the static magnetization, and $\mathbf{m} << 1$ is the small dynamic deviation of the magnetization from its equilibrium position. Using this representation in Eq. 4, we derive the following expression for the SW vector and amplitudes

$$-i\omega_{k_x}\mathbf{m}_{k_x,p} = \boldsymbol{\mu} \times \sum_q \hat{\boldsymbol{\Omega}}_{k_x,pq} \cdot \mathbf{m}_{k_x,q} \tag{5}$$

which is the Fourier representation (in time and x coordinate) of the linearized LL equation. Here, $\boldsymbol{\mu}$ is the unit vector along the direction of the static magnetization; indices $p, q = 1, 2$ enumerate waveguides; and the tensor $\hat{\boldsymbol{\Omega}}_{k_x,pq}$ has the form

$$\hat{\boldsymbol{\Omega}}_{k_x,pq} = \gamma(B + \mu_0 M_s \lambda^2(k_x^2 + \kappa^2))\delta_{pq}\hat{\mathbf{I}} + \omega_M \hat{\mathbf{F}}_{k_x}(d_{pq}) \tag{6}$$

where B is the static internal magnetic field, which in our case is considered to be equal to the external magnetic field due to the negligible demagnetization along the x direction, d_{pq} is the distance between the centers of the two waveguides (that is, $d_{pp} = 0$, $d_{12} = -d_{21} = w + \delta$), δ is the gap between the waveguides of width w, $\lambda = \sqrt{2A/(\mu_0 M_s^2)}$ is the exchange length, δ_{pq} is the Kronecker delta function, $\omega_M = \gamma\mu_0 M_s$, μ_0 is the vacuum permeability, γ is the gyromagnetic ratio, and $\hat{\mathbf{I}}$ is the identity matrix. Note that, due to the effective dipolar boundary conditions (*34*, *35*) at the lateral boundaries of the waveguides, the width profiles of the collective SW modes will be, in general, partially pinned, resulting in a nonuniform width profile of the fundamental SW mode of the waveguide $m(y) \sim \cos(\kappa y) = \cos(\pi y/w_{\text{eff}})$. This nonuniformity is taken into account by the effective wave number $\kappa = \pi/w_{\text{eff}}$, where w_{eff} is the effective width of the waveguide (see illustration in Fig. 1C). In general, the effective width of the waveguides w_{eff} can be substantially larger than the nominal waveguide width w when the effective pinning decreases (see Fig. 1C). The influence of the dynamical magneto-dipolar interaction (both intra- and inter-waveguides) in Eq. 6 is described by the tensor $\hat{\mathbf{F}}_{k_x}$, which is convenient to calculate using a Fourier-space approach, developed by Beleggia *et al.* (*38*), namely

$$\hat{\mathbf{F}}_{k_x}(d) = \frac{1}{2\pi}\int \hat{\mathbf{N}}_k e^{ik_y d} dk_y \tag{7}$$

$$\hat{\mathbf{N}}_k = \frac{|\sigma_k|^2}{\tilde{w}} \begin{pmatrix} \frac{k_x^2}{k^2} f(kt) & \frac{k_x k_y}{k^2} f(kt) & 0 \\ \frac{k_x k_y}{k^2} f(kt) & \frac{k_y^2}{k^2} f(kt) & 0 \\ 0 & 0 & 1 - f(kt) \end{pmatrix} \tag{8}$$

where $f(kt) = 1 - (1 - \exp(-kt))/(kt)$, $k = \sqrt{k_x^2 + k_y^2}$, t is the waveguide thickness, $\sigma_k = \int_{-w/2}^{w/2} m(y) e^{-ik_y y} dy$ is the Fourier transform of the SW profile across the width of the waveguide, and $\tilde{w} = \int_{-w/2}^{w/2} m(y)^2 dy$ is the normalized constant of the mode profile $m(y)$. For $k = 0$, one should calculate the corresponding limit of $\hat{\mathbf{N}}_k$. In the case $d = 0$, the tensor $\hat{\mathbf{F}}_{k_x}(0)$ coincides with the dipolar self-interaction inside the waveguide. $\hat{\mathbf{F}}_{k_x}(d)$ is the dipolar interaction between the waveguides. In the case of an almost uniform SW profile $m(y) = 1$, which is realized if the waveguide size is close to or smaller than the material exchange length λ or if the effective boundary conditions are free (that is, $w_{\text{eff}} \to \infty$), the Fourier transform is described by the function $\sigma_k = w\,\text{sinc}(k_y w/2)$ and $\tilde{w} = w$. For any other spatially symmetric mode with the profile $m(y) \sim \cos(\kappa y)$, the Fourier transform σ_k can be evaluated as

$$\sigma_k = 2\left[\frac{k_y \cos(\kappa w/2)\sin(k_y w/2) - \kappa \cos(k_y w/2)\sin(\kappa w/2)}{k_y^2 - \kappa^2}\right],$$

$$\tilde{w} = \frac{w}{2}(1 + \text{sinc}(\kappa w)) \tag{9}$$

Noting that the tensor $\hat{\mathbf{F}}_{k_x}(d)$ is diagonal and real (as long as the static magnetization is directed along one of the symmetry axes of the waveguide), we can obtain simple explicit expressions for the SW dispersion relations of the waveguide SW modes. The dispersion relation for the SW mode in an isolated waveguide is

$$f_0(k_x) = \frac{1}{2\pi}\sqrt{\Omega^{yy}\Omega^{zz}} = \frac{1}{2\pi}\sqrt{(\omega_H + \omega_M(\lambda^2 K^2 + F_{k_x}^{yy}(0)))(\omega_H + \omega_M(\lambda^2 K^2 + F_{k_x}^{zz}(0)))} \tag{10}$$

The dispersion relation for two coupled waveguides (two modes) is

$$f_{1,2}(k_x) = \frac{1}{2\pi}\sqrt{(\Omega^{yy} \pm \omega_M F_{k_x}^{yy}(d))(\Omega^{zz} \pm \omega_M F_{k_x}^{zz}(d))} \tag{11}$$

where $\Omega^{ii} = \omega_H + \omega_M(\lambda^2 K^2 + F_{k_x}^{ii}(0))$, $i = y, z$, $\omega_H = \gamma B$, $\omega_M = \gamma\mu_0 M_s$, and $K = \sqrt{k_x^2 + \kappa^2}$. Noting that the magneto-dipolar interaction between the waveguides is small compared to the dipolar self-interaction inside the waveguide, the dispersion relations of the two collective

modes (symmetric and antisymmetric) in a pair of coupled waveguides can be approximated as

$$f_{1,2}(k_x) \approx f_0(k_x) \pm \Delta f/2 \quad (12)$$

where the frequency separation between the symmetric and antisymmetric collective modes is given by

$$\Delta f = \omega_M \frac{\Omega^{zz} F_{k_x}^{yy}(d) + \Omega^{yy} F_{k_x}^{zz}(d)}{4\pi^2 f_0(k_x)} \quad (13)$$

Equation 13 describes the dependence of the frequency separation between the symmetric and antisymmetric modes on all the geometrical and material parameters of the system consisting of two coupled waveguides. In general, Δf increases with an increase in dynamic magneto-dipolar interaction between the waveguides. This increase can be realized by decreasing the separation between the waveguides or by an increase of the thickness-to-width aspect ratio of the waveguides. In addition, Δf significantly depends on the saturation magnetization of the used materials. If the wave number of the excited SW, as well as the spin-pinning conditions (effective width w_{eff}), is fixed, then Δf can be approximated as $\Delta f \propto \omega_M \propto M_s$ in both the dipolar and exchange regions and is independent of the applied external field. As shown by Eq. 2, the coupling length $L = v_{gr}/(2\Delta f)$ is proportional to the ratio between the SW velocity and the frequency separation. Because in dipolar approximation the velocity $v_{gr} \propto M_s$ is practically proportional to the saturation magnetization, the coupling length L is independent of the choice of the material. Thus, the use of yttrium iron garnet (YIG), which has a smaller value of M_s compared to metallic materials, is preferable for dipolar waves due to the longer SW lifetimes in this material. In contrast, in the exchange-dominated region, the SW dispersion relation can be approximated as $f = \frac{1}{2\pi}\omega_M \lambda^2 k^2$, and the group velocity $v_{gr} = 2\pi\frac{\partial f}{\partial k} = 4\gamma\frac{A}{M_s}k$ is inversely proportional to the saturation magnetization. Thus, the exchange waves in metallic magnetic materials with large M_s are slower and, consequently, have smaller propagation decay lengths in comparison to YIG (even if to neglect much larger SW lifetimes in YIG). However, the coupling length $L \propto \frac{A}{M_s^2} \propto \lambda^2$ in the exchange region is smaller in the materials with high M_s, and another mechanism can be used to enhance the coupling between the SW waveguides as discussed later.

The developed analytical theory represents a method to calculate the characteristics of the magnonic SW couplers that are relatively simple and intuitive, compared to the traditional micromagnetic simulations. In the following, the analytic results are directly compared to the results of micromagnetic simulations.

RESULTS

Model and simulations

The structure of a directional coupler is schematically shown in Fig. 2A. Two parallel waveguides (length of 100 μm, width w ranging between 100 and 300 nm, and thickness t in the range of 10 to 50 nm) are placed laterally parallel with a gap δ (ranging between 10 and 100 nm). The numerical modeling of this structure is performed using the MuMax3 (*39*) micromagnetic package with the following parameters of a YIG nanometer-thick film (*10*, *40*): saturation magnetization $M_s = 1.4 \times 10^5$ A/m, exchange constant $A = 3.5$ pJ/m, and Gilbert damping $\alpha = 2 \times 10^{-4}$. In our numerical simulations, the Gilbert damping at the ends of the waveguides is set to exponentially increase to 0.5 to eliminate SW reflections at the waveguide ends [experimentally, this can be realized using tapered edges (*30*) or by placing a normal metal on top of the waveguide edges to use the phenomena of spin pumping (*6*, *10*)]. Because of the ultralow Gilbert damping of YIG, the SW propagation distances in YIG waveguides reach up to dozens of micrometers (*10*, *14*, *41*, *42*), which opens up the possibility for the realization of complex integrated SW circuits. A small external magnetic field $B_{ext} = 10$ mT is applied along the long axis of the waveguides (x direction in Fig. 2). To excite a propagating SW in one of the waveguides, we applied a sinusoidal magnetic field $b_y = b_0\sin(2\pi ft)$ at the center of the second waveguide over an area of 20 nm in length (see yellow area shown in Fig. 2A), with the oscillation amplitude $b_0 = 1$ mT and a varying microwave frequency f.

Splitting of SW dispersion curves due to the dipolar coupling between waveguides

Figure 2B shows a snapshot of the dynamic magnetization profiles in the coupled waveguides with the following parameters: width $w = 100$ nm, thickness $t = 50$ nm, and gap δ = 100 nm. The frequency of the excited SW in this case was 2.96 GHz, corresponding to a wave number $k_x = 0.02872$ rad/nm. It can be seen that the energy of the SW, excited in waveguide #2, is transferred completely to waveguide #1 after propagation over the coupling length L (see Fig. 2B). Figure 2 (C and D) shows the variations of the SW power in the two coupled waveguides as a function of the propagation distance x for the case of zero damping (Fig. 2C) and for the case of a typical damping of YIG film ($\alpha = 2 \times 10^{-4}$) (Fig. 2D). The coupling length of $L = 12$ μm can be extracted from Fig. 2 (C and D). Note that the SW wavelength in our studies is of the order of 100 nm. The simulation performed for the damping-free waveguides shows the lossless oscillations of the SW energy between the waveguides. The blue line is a fit to the data using the dependence $P_1 = P_{in}\sin^2(x\pi/(2L))$, where P_{in} is the power launched into waveguide #2 and P_1 is the power in waveguide #1. In the case where realistic SW damping is taken into account, the SW power gradually decreases, as expected. The results can be fitted by a similar model that includes the damping term $P_1 = P_{in}\sin^2(x\pi/(2L))\exp(-|2x|/x_{freepath})$, where $x_{freepath} = 88$ μm is the exponential decay length, which is in good agreement with the analytical theory.

Figure 2E shows the dispersion characteristics of the two lowest width modes of a single isolated waveguide, and Fig. 2F shows the similar dispersion curves for a pair of the waveguides coupled across a gap of δ = 10 nm. The color maps were calculated by micromagnetic simulations, whereas the black dashed lines for the lowest width SW mode were obtained using the analytic equations (Eqs. 10 and 11) for the single waveguide and the coupled waveguides, respectively.

It is seen that the dispersion curve corresponding to the lowest width mode of a single waveguide splits into two modes: antisymmetric (as) (top) and symmetric (s) (bottom) (see Figs. 1C and 2F). This splitting is caused by the dipolar interaction between the waveguides. The oscillations of the SW energy in the coupled waveguides can be interpreted as an interference of the symmetric and antisymmetric SW modes (*28*–*30*). These two SW modes have the same frequency but different wave numbers and, therefore, different phase velocities. Thus, these modes accumulate a phase difference during their propagation in the waveguides. When the accumulated phase difference is equal to π, the superposition of the two modes results in a destructive interference in one of the waveguides and in a constructive interference in the other one. The

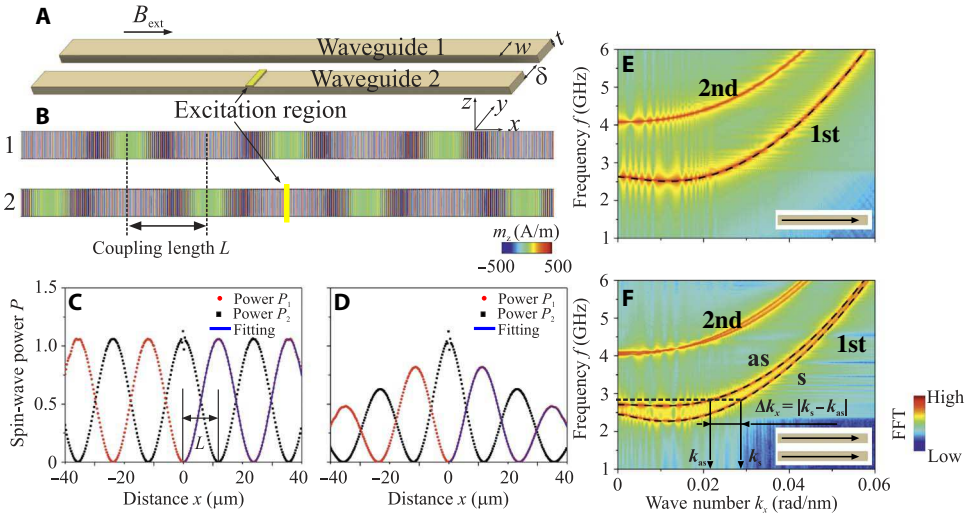

Fig. 2. Energy transfer in dipolarly coupled waveguides. A schematic view of the dipolarly coupled SW waveguides (**A**) and a snapshot of the SW profile excited in them (**B**). The excitation antenna (shown in yellow) is located in the center of one of the waveguides. Variation of the SW power in both waveguides as a function of propagation distance *x* for the case of zero SW damping (**C**) and for the typical damping in YIG film (**D**). (**E**) Dispersion characteristics of the two lowest width SW modes in a single isolated waveguide. (**F**) Similar dispersion curves for a pair of coupled waveguides. A color map represents the results of our numerical simulations, whereas the dashed lines represent the analytical theory. Splitting of the SW dispersion curves into antisymmetric (as) (top) and symmetric (s) (bottom) branches due to the dipolar coupling between the waveguides is shown.

SW energy is completely transferred from one waveguide to the other after propagation for a coupling length *L*. Analogously, the energy is transferred back to the first waveguide after the further propagation for the same distance *L*, and the process is periodic (see movie S1). Note that the complete SW energy periodic exchange between the coupled waveguides is possible only if the waveguides are identical, have parallel or antiparallel static magnetization, and experience the same internal magnetic field. In other cases, the SW energy is also transferred on a distance *L*, but the transfer is incomplete (*43*).

Coupling length

Figure 3 shows the dependence of the coupling length *L* on the geometrical parameters of the waveguides: the gap size δ (Fig. 3A), the thickness *t* (Fig. 3C), the width *w* (Fig. 3D) of the waveguides, and, on the SW, wave number k_x (Fig. 3B). In general, it can be seen that the increase of the dipolar coupling between the waveguides results in a decrease of *L*. The coupling between the waveguides is increased by a decrease of the gap δ between the waveguides, by a decrease in their width *w*, or by an increase in their thickness *t*. Note, also, that the coupling strength is decreased with increasing SW wave number k_x due to the decreased dipolar interaction for short-wavelength exchange SWs. The latter is a challenge that should be addressed in the design of future nanomagnonics devices operating with SWs on the nanometer wavelength scale. One way to overcome this difficulty is to further decrease the gap between the waveguides. Another possible way to increase the coupling between the waveguides and, thus, to decrease the lateral sizes of the directional coupler is to fill the gap between the waveguides with another magnetic material [see, for example, the study of Wang *et al.* (*44*)]. For this purpose, it is preferable to use magnetic materials with higher values of M_s to ensure that the SW excitation in this material has higher frequencies and does not disturb the operational characteristics of the directional coupler (these studies are beyond the scope of the present work). The results obtained from the micromagnetic simulations (circle points) and from the analytical theory (lines) are consistent with those in Fig. 3. In the waveguides with a width $w > 150$ nm, the SW profile across the width becomes essentially nonuniform due to dipolar pinning (*34*, *35*), and the micromagnetically calculated SW profiles (in an isolated waveguide) are used for the calculation of the geometric form factor σ_k.

In the course of our simulations, a single-frequency SW was excited in one of the waveguides, and the width profile of this SW mode was extracted from the results of numerical simulation. The function $m_z(y) = A_0 \cdot \cos(\pi y / w_{eff})$, where A_0 is the amplitude, was used to fit the numerically calculated width profile of the SW mode to obtain the effective waveguide width w_{eff}. Then, this effective width was inserted into Eq. 9 for analytic calculations. The inset in Fig. 3D shows the dependence of the effective width on the geometrical width *w* of the waveguides. The effective width strongly increases with the decrease in *w*, which corresponds to the gradual decrease of the effective dipolar pinning at the lateral edges of the waveguides (*34*, *35*).

Antiparallel magnetization configuration

In the previous sections, it was assumed that a small external bias magnetic field was applied along the *x* direction to orient the static magnetization along the waveguides' long axes. However, in nanoscale waveguides, the static magnetization orients itself parallel to the waveguides spontaneously without any external field due to the strong shape anisotropy of the elongated nature of a waveguide. Moreover, in the absence of an external field, waveguides can exist in two stable magnetic configurations—with parallel and antiparallel static magnetizations. The analytical calculations show that the SW dispersion and, therefore, the coupling length depend significantly on the static magnetization configuration. This is a result of the gyrotropic motion of the magnetization vector—in the parallel configuration, the magnetization vectors of both waveguides rotate in the same direction, whereas in the antiparallel configuration, they rotate in the opposite directions, which leads to a different dynamic magneto-dipolar interaction between the waveguides. In particular, for the antiparallel configuration of the

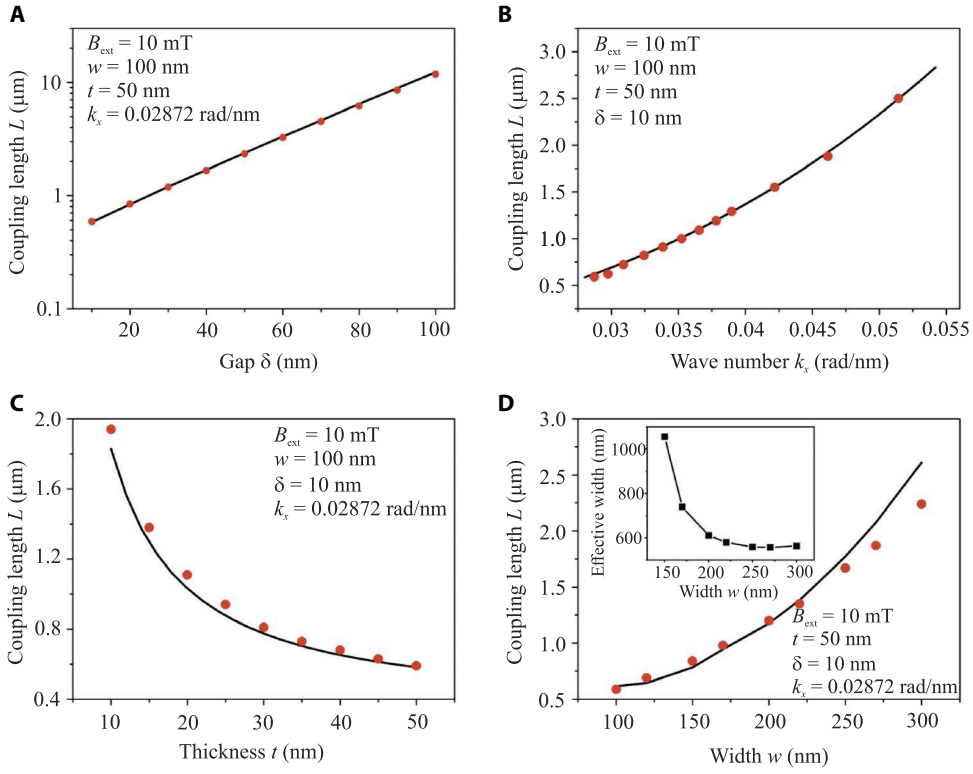

Fig. 3. Coupling length. The coupling length L, that is, the SW propagation length over which the SW energy is transferred from one waveguide to the other, is shown as a function of (**A**) the separation δ between the waveguides, (**B**) the longitudinal wave number k_x, (**C**) the thickness t of the waveguides, and (**D**) the width w of the waveguides. These results were obtained by means of numerical simulations (symbols) and analytical calculations (lines). The parameters for each particular case are shown directly inside the panels. The inset in (D) shows the dependence of the effective width w_{eff} of the waveguide on the nominal width w (the line is a guide for the eye). The decrease in the waveguide width results in the reduction of the effective dipolar pinning at the lateral edges of the waveguides and in the corresponding increase of the effective waveguide width.

waveguide static magnetizations, the splitting of the dispersion relation of the symmetric and antisymmetric collective modes is given by

$$\Delta f = \omega_M \frac{\Omega^{zz} F_{k_x}^{yy}(d) - \Omega^{yy} F_{k_x}^{zz}(d)}{4\pi^2 f_0(k_x)} \quad (14)$$

This equation is substantially different from the splitting Eq. 13 that takes place in the case of parallel static magnetization of the coupled waveguides. As one can see from Fig. 4 (A and B), the frequency splitting is stronger for the antiparallel magnetization configuration, which results from the stronger interaction of the oppositely precessing dynamic magnetizations in the two coupled waveguides. Consequently, the coupling length for the antiparallel configuration is always smaller than that for the parallel magnetization configuration, as one can see from the dependence of the coupling length L on the gap δ and on the SW wave number k_x shown in Fig. 4, C and D, respectively.

Design of a directional coupler

The dipolarly coupled SW modes in parallel waveguides have a large potential for applications. The functionality of a microwave signal processing device based on two laterally parallel coupled waveguides depends on the ratio between the coupling length L and the length of the coupled waveguides L_W. Thus, according to Eq. 3, if $L_W = (2n + 1)L$, where n is an integer value, then the entire energy will be transferred from one waveguide to the other, and the directional coupler can be used as a connector of magnonic conduits. If $L_W = (n + 1/2)L$, then the coupler can be used as an equal divider (3 dB in each beam pass) for microwave power. Taking into account that the coupling length L strongly depends on the SW wave number k and, consequently, on the signal frequency, the directional coupler can be used as a frequency separator. Finally, the variation of the external bias magnetic field and/or of the direction of static magnetization in one of the coupled waveguides allows the switching of the functionality of the directional coupler having a fixed length L_W and fixed signal frequency.

One of the challenging tasks in the practical realization of a directional coupler is the design of the inputs (outputs) to (from) the coupled SW waveguides that are needed to precisely define the L_W/L ratio [note, for example, the absence of such inputs and outputs in the studies of Sadovnikov and colleagues (*30*–*32*)]. The design of directional couplers proposed here is somewhat analogous to the design of optical directional couplers (*29*) but needs a substantial modification because of the anisotropy of the SW dispersion laws and their qualitative dependence of the orientation of the static magnetization in an SW waveguide (*21*, *45*). Moreover, the SW spectra typically have a multimode character, which can significantly complicate the SW microwave signal processing (*19*). Most of these problems are automatically solved, when the sizes of the magnonic signal processing devices are scaled down to below a micrometer. In this case, the frequencies of the SW modes are well separated due to the strong exchange interaction that shifts the frequency of the higher-order thickness and width modes by several gigahertz (see, for

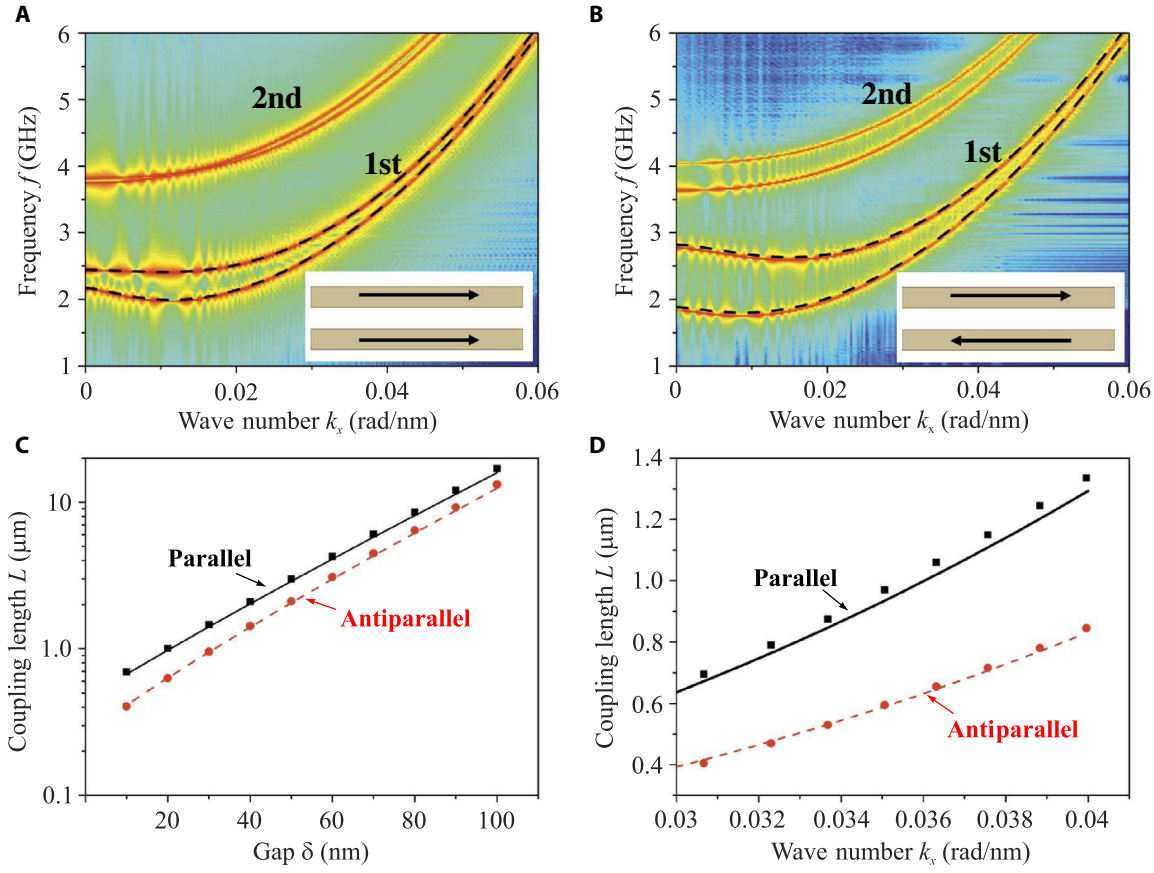

Fig. 4. Dependence on the static magnetization configuration. Dispersion characteristics of the lowest SW width modes in coupled waveguides for the cases of parallel (**A**) and antiparallel (**B**) orientation of the static magnetizations of the waveguides (see insets). Dashed lines show the results of the analytic theory. The waveguide parameters are as follows: width w = 100 nm, thickness t = 50 nm, and gap width δ = 10 nm. Coupling length as a function of the gap width δ (k_x = 0.03066 rad/nm) (**C**) and as a function of the longitudinal wave number k_x (δ = 10 nm) (**D**) for parallel (black squares and solid black lines) and antiparallel (red circles and dashed red lines) static magnetization configurations. The symbols show the numerical results, whereas lines correspond to the results calculated analytically.

example, Fig. 2E). Moreover, as described above, the strong shape anisotropy of the elongated SW waveguides makes the waveguides static magnetization parallel to the long axis of the waveguide and, therefore, along the direction of the SW propagation even in the presence of a small external bias magnetic field (see black arrows in Fig. 5A showing the direction of static magnetization). This quasi-isotropic condition for the SW propagation is one of the big advantages of the nanosized magnonic conduits when compared to the similar systems of the micro- and macroscale. The angle between the sections of the directional coupler is chosen to be 20°, as shown in the figure. This angle is small enough to show a good SW transmission through the bent point of the SW waveguide. Additional simulations are performed using the upper left region of the directional coupler (the region that contains two bents of the waveguide and is marked by dashed lines in Fig. 5A, bottom panel) and compared to the reference straight waveguide. The results show that the reflection weakly increases with the increase in the SW wave number but stays below 5% for the design shown in Fig. 5A.

Therefore, the structure shown in Fig. 5A, which is analogous to the directional coupler used in integrated optics (*29*), is also suitable for the realization of an SW directional coupler but on the nanometer scale. The main drawback of such a design is that the corners of the structure (marked with red circles in Fig. 5A) could act as secondary SW sources, thus disrupting the operational characteristics of the device. To minimize these distortions, we introduced a translational shift d_s = 100 nm between the beams in the practical model of the proposed directional coupler, as shown in Fig. 5A. In the absence of this shift (d_s = 0 nm), the transmission of the SW power to the other waveguide drops down from 99.6 to 97.9% (for the case illustrated in Fig. 6A). The increase of the shift d_s > 100 nm, practically, does not influence the transmission anymore if the length L_W is fixed. The improvement of the transmission characteristics is independent of the direction of the translational shift. In the following studies, we fixed the width of the waveguides to w = 100 nm, the thickness to t = 50 nm, and the gap between the waveguides to δ = 30 nm. The length of the coupled waveguides L_W was fixed to be equal to $L_W = D - d_s$ = 4900 nm.

Figure 5B shows the normalized output power in the first beam pass $P_{1\ out}/(P_{1\ out} + P_{2\ out})$ as a function of the SW wave number k_x. The symbols represent the results of the micromagnetic simulations, and the lines are obtained from the analytical theory for the parallel (black) and antiparallel (red) configuration of the waveguides' static magnetizations, respectively.

Note that, despite the fact that the directional coupler as a whole was studied by micromagnetic simulations, although only the parallel parts (of the length L_W) of the coupled waveguides were considered in the

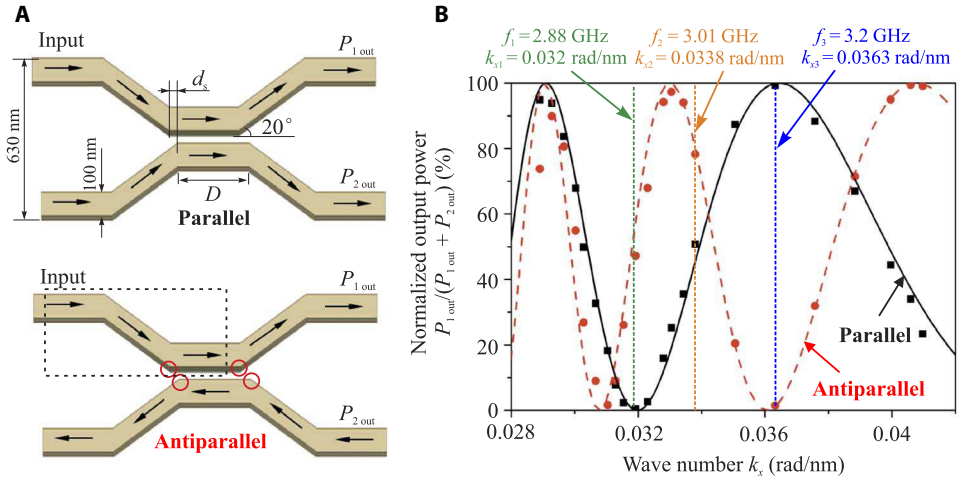

Fig. 5. Reconfigurable SW directional coupler. (**A**) Schematic view of the parallel and antiparallel magnetization configuration of the directional coupler. The widths of the waveguides are w = 100 nm, thickness is t = 50 nm, and gap is δ = 30 nm; the angle between the coupler waveguides is 20°; and the working length of the coupled waveguides is $L_W = D - d_s$ = 4900 nm. The arrows show the direction of the static magnetization. The SWs are excited in the first beam pass of the directional coupler marked as "Input." (**B**) Wave number dependence of the normalized power at the output of the first beam pass $P_{1\,out}/(P_{1\,out} + P_{2\,out})$ of the directional coupler. The symbols and lines were obtained by micromagnetic simulations and the analytical theory for parallel (black squares and solid black line) and antiparallel (red circles and dashed red line) configurations, respectively. The vertical dashed lines indicate the wave numbers (and corresponding frequencies), which are chosen for the demonstration of different functionalities of the directional coupler in Fig. 6.

framework of the analytical theory, the difference in the results is very small. This is an indication of the high efficiency (small SW reflections) of the proposed directional coupler design. It can be seen in Fig. 5 that the operational characteristics of the directional coupler can be easily tuned by the variation of the SW wave number (that is, by the frequency of the input microwave signal). Moreover, this tuning is different for parallel and antiparallel configurations of the static magnetization that provides an additional degree of freedom to the utilization of the coupler. In the following, we choose three different values of the SW wave number, which are shown by vertical dashed lines in Fig. 5B, and perform separate simulations for the case of a single-frequency input signal. The design and all the sizes of the directional coupler are kept the same for all the simulations shown in Fig. 6. There is no biasing magnetic field applied in all cases shown in Fig. 6 excluding Fig. 6 (H and J).

Functionalities of a directional coupler

Figure 6 shows the color maps of the SW amplitude (represented by the variable component of the dynamic magnetization m_z) in a directional coupler for different input frequencies and, consequently, wave numbers. Because it is expected from the results shown in Fig. 5B, the SW of the frequency f_1 = 2.88 GHz is almost fully transferred to the second waveguide. After a few oscillations between the waveguides, 99.6% of the output SW energy (here, we show the fraction of the output SW power between two outputs) is detected at the second pass of the device in our simulations. The coupling length (L = 1630 nm in this case) satisfies the ratio $L_W = 3 \times L$. Thus, this directional coupler can be used to effectively connect two magnonic conduits. If the SW of the same frequency is excited in the other pass of the coupler, then the SW energy will be transferred into the opposite pass in a similar way.

The situation is different for the SW of the frequency f_3 = 3.2 GHz (see Fig. 6C) that corresponds to a longer coupling length of L = 2450 nm. The length of the waveguides is $L_W = 2 \times L$ in this case (see also Fig. 5B), and the SW energy is transferred back to the input pass of the directional coupler. This means that the directional coupler can be used as a frequency separator (multiplexer): If SWs of different frequencies f_1 and f_3 are simultaneously excited in the same beam pass of the waveguide, then the SW of frequency f_1 will exit from one pass of the coupler, whereas the signal of frequency f_3 will exit from the other pass, as shown in Fig. 6 (D to F) (see also movie S2). Figure 6B shows that the directional coupler can be used as a 3-dB power divider in which half of the energy is transferred to the second pass of the coupler and half of the energy stays in the first pass. A propagating SW of the frequency f_2 = 3.01 GHz corresponding to L = 1960 nm has been excited in this case to ensure the condition $L_W = 2.5 \times L$. The ratio between the output energies in both beam passes of the waveguide can be easily tuned by the frequency of the input signal.

Furthermore, the ratio between the output powers can be adjusted by shifting the dispersion curves up or down using an applied external magnetic field. An SW of the frequency f_3 = 3.2 GHz has a coupling length L = 2450 nm (unbiased case). In this case, the SW energy is transferred back to the same input pass of the directional coupler (see Fig. 6G). When the external bias magnetic field is increased to 7.1 mT, the coupling length decreases to 1960 nm, and the directional coupler acts as a 3-dB power divider (see Fig. 6H). The continuing increase of the bias field to 12 mT results in the coupling length further decreasing to 1630 nm, and in such a situation, most of the SW energy is transferred to the second pass of the directional coupler, as shown in Fig. 6I. The energy of the propagating SW can be switched from one pass to the other during a few nanoseconds using the application of an abrupt step in the external bias field. Movie S3 shows the situation in which the biasing magnetic field B_{ext} is changed from 0 to 12 mT within 10 ns. Because the magnetization ground state is not changed in this case (as opposed to the process of the switching of the magnetization direction discussed further), the switching time is limited only by the time that the SW needs to pass the directional coupler (around 20 ns in our simulations).

Finally, we study the case when an SW of frequency f_3 is excited (see Fig. 6J), but the relative orientation of the static magnetizations in the

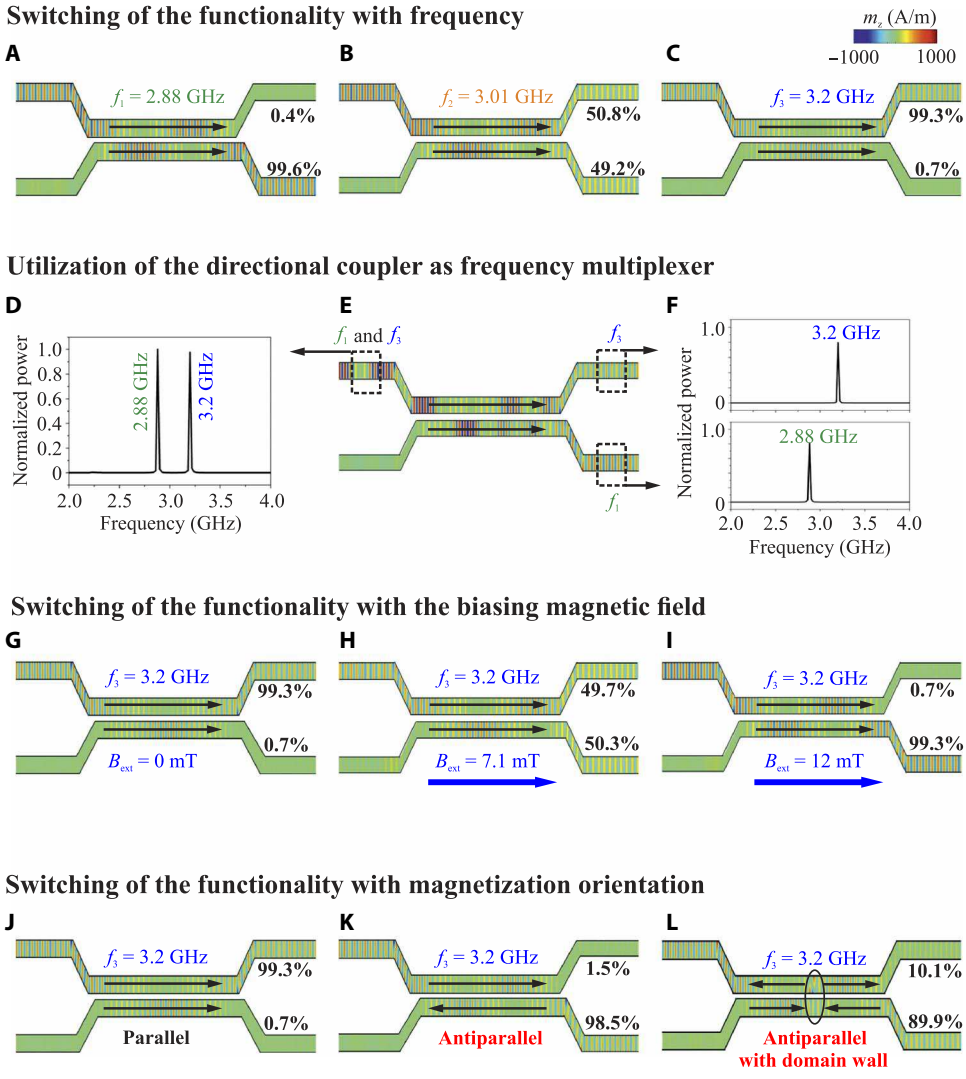

Fig. 6. Dynamically reconfigurable SW directional coupler. (**A** to **C**) Switching of the device functionality by changing the signal frequency. Directional coupler acts as a connector of magnonic conduits, as a 3-dB power divider, or as a simple transmission line (delay line). (**D** to **F**) Utilization of the directional coupler as a frequency separator (multiplexer). The directional coupler can be used as a frequency multiplexer. SWs of two frequencies simultaneously excited in the first beam pass of the coupler will reach different output beams. (**G** to **I**) Switching of the device functionality by changing the bias magnetic field. The ratio of the output powers in two beam passes can be changed by the variation of the bias magnetic field. The demagnetization fields were taken into account in the simulations. (**J** and **K**) Switching of the device functionality by changing the static magnetization orientation. Switching the relative orientation of the static magnetization in two beam passes leads to the switching of the output signal between the beam passes. (**L**) Even in the case when the remagnetization process leads to the formation of a domain wall in the device beam passes, the main part (90%) of the output signal power is still transferred from the upper to the lower beam pass. The SW amplitude is shown by a color map. Note that the width of the waveguides is constant in all parts of the directional coupler, as shown in Fig. 5A. The structures are compressed in the direction along the waveguide for a better illustration of the coupling effects.

beam passes has been switched from parallel to antiparallel (see Fig. 6K). As expected, on the basis of the results presented in Fig. 5B, most of the SW energy is transferred in that case from one pass of the directional coupler to the other one due to the shorter coupling length L for the antiparallel magnetization configuration (L = 1640 nm in this case satisfies the condition $L_W = 3 \times L$). Thus, the proposed directional coupler turns out to be fully dynamically reconfigurable and can be used as an effective and fast switch and/or multiplexer (*9*).

Obviously, the operational frequency of the device can be easily varied with the length of the directional coupler L_w by the geometry of the waveguides that defines the coupling length L or by the external bias magnetic field. However, it is important to note that the maximum operating power of such a frequency multiplexer is limited by different nonlinear SW phenomena (*18*, *30*, *45*).

Switching of the orientation of static magnetization in a directional coupler

Here, we would like to discuss the practical realization of the switching of the relative orientation of the static magnetizations in the passes of the directional coupler (see Fig. 4). Taking into account a very short separation distance between the parallel passes of the coupler, it is difficult to remagnetize the passes of the coupler independently using external magnetic fields. Instead, here, we propose to use a method similar to the one used in previous studies (*12*, *46*–*48*) for the switching of

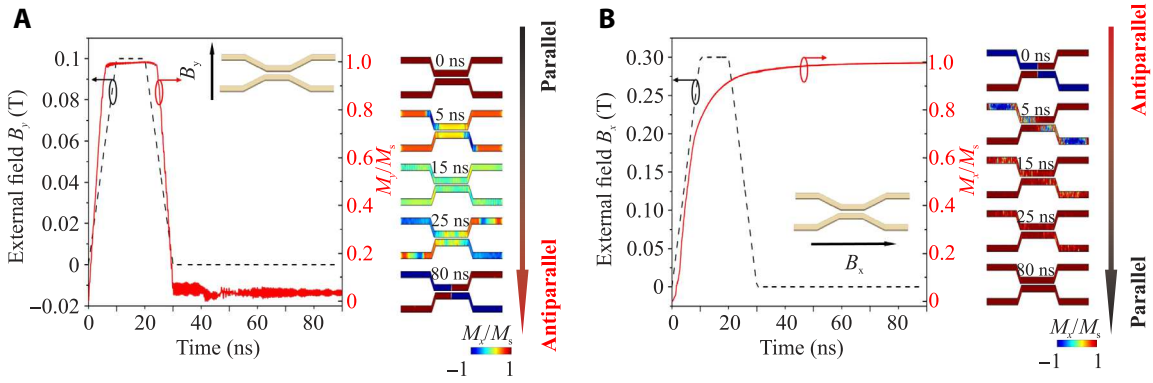

Fig. 7. Switching of the directional coupler. (**A**) Application of a magnetic field pulse in the direction transverse to the coupled waveguide direction results in the switching of the magnetization from the parallel to the antiparallel state (see color map in the right panels for M_x component). Two domain walls are formed in the centers of the coupler beam passes in such antiparallel magnetization configuration. (**B**) Profile of the longitudinal magnetic field pulse for the switching of the directional coupler magnetization back into the parallel state. The magnetization configuration is shown in the same way as in (A).

the magnetic state in arrays of dipolarly coupled magnetic nanodots. Namely, we apply a short (~20 ns) magnetic field (0.1 T) pulse in the perpendicular direction (*y* direction), which temporarily magnetizes both waveguides in the *y* direction (Fig. 7A).

Then, the applied field is decreased to zero within 10 ns. This evolution not only allows the static magnetization in the coupler to be spontaneously directed along the long axes of the waveguides (see movie S4) but also results in the excitation of parasitic SWs in the structure (see the long tail in the M_y characteristics). In general, the device is ready for operation after a time period exceeding at least one SW life cycle, which, in our case, is equal to 252 ns (for the 3-GHz frequency).

However, even 50 ns after the bias field has been turned off, one can see that the magnetization distribution in the directional coupler assumes the form shown in the right panels of Fig. 7A. Each pass of the waveguide contains a domain wall in the center of the structure (due to the energy minimum condition) and is therefore separated into two regions with opposite directions of the static magnetization. The magnetization orientations in both regions are antiparallel to each other as desired.

To prove that the domain walls do not substantially disturb the operational characteristics of the device, we performed additional simulations for a single SW waveguide with the same domain wall structure and showed that the SW reflection coefficient due to the domain wall is only 3%. Figure 6L demonstrates that the magnetization configuration with the presence of the domain walls does not have much influence on the operational characteristics of the directional coupler when compared to the ideal antiparallel aligned magnetization configuration shown in Fig. 6K.

To switch the magnetization configuration of the directional coupler back to the parallel state, we applied a field of 0.3 T in the *x* direction (parallel to the waveguides), as shown in Fig. 7B. The magnetic field is switched on again for 30 ns with a rise and fall time of 10 ns. Note that these time intervals are important because the switching of the magnetic field for a shorter period will not necessarily result in the switching of the magnetization configuration. The magnetization orientation is shown in the same way as in Fig. 7A. One can see that approximately 50 ns after the external field was switched off, the directional coupler stays in its original parallel magnetization configuration (see movie S5). Figure 6J shows the SW amplitude in this case, and one can see that the SW energy reaches the same beam pass in which it was originally excited. Thus, the proposed methodology allows the realization of the SW switch.

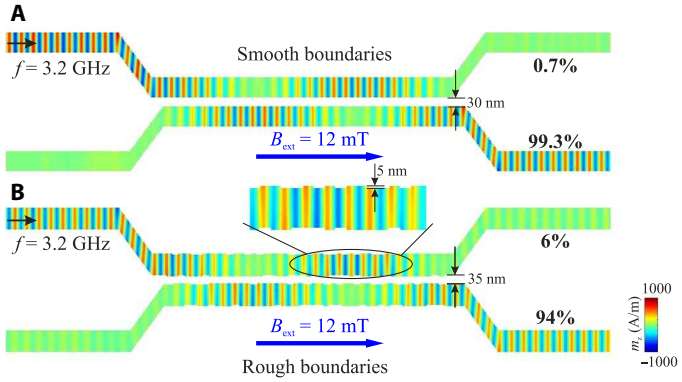

Fig. 8. Influence of rough boundaries on the characteristics of a directional coupler. A snapshot of the SW profile in (**A**) smooth boundaries and (**B**) rough boundaries.

Robustness of the directional coupler characteristics

We would like to mention that the simulations presented here were performed without taking into account temperature, that is, for zero effective temperature. Additional numerical simulations, identical to those shown in Fig. 6A (at an SW frequency of 2.88 GHz), were performed at an effective temperature of 300 K (using the embedded MuMax3 package) to explore the influence of temperature on the characteristics of the directional coupler (see movies S6 and S7). Only a small difference between the operational characteristics of the device was obtained for different temperatures: The output power of the device is 99.6% at zero temperature and 86.3% at room temperature. The difference is mainly caused by a slight shift of the dispersion characteristics of SWs due to the decrease in the saturation magnetization (*49*) that results, consequently, in a change of the coupling length. This behavior is analogous to the temperature-induced change of the coupling length in optical directional couplers due to the change of the refractive index (*29*, *50*). The role of temperature can be decreased by an adjustment of the coupling length via a slight variation of the signal frequency. The output power of the device can be increased to 94.5% at room temperature by slightly decreasing the frequency to 2.84 GHz (see movie S8).

Finally, we would like to discuss the influence of rough boundaries at the edges of the SW waveguides (that might result from the fabrication

process) on the characteristics of a magnonic directional coupler. Additional numerical simulations, similar to those shown in Fig. 6I (in the presence of a weak external magnetic field of 12 mT), were performed with rough boundaries (see Fig. 8B). Five-nanometer-wide and randomly defined long (from 50 to 400 nm to be comparable to the SW wavelength) rectangular magnetic elements are additionally introduced on both sides of each SW waveguide to act as roughness. The introduction of the roughness results in the increase of the average width of the waveguides. To compensate it, we increased the gap δ from 30 to 35 nm. Only a small difference in the operational characteristics of the directional coupler was found for different boundary conditions: The output power of the device is 99.3% for the smooth boundaries and 94% for the rough boundaries. These robust operational characteristics are due to the "diluted" SW dispersion spectra in the nanoscale waveguide shown in Fig. 2F, in which the frequencies of higher thickness and width modes are separated by several gigahertz. As a result, the elastic two-magnon scattering damping mechanism is absent (*19*, *21*). This is an additional advantage given to the directional coupler by its nanometer sizes.

CONCLUSION

In conclusion, a practical design of a nanoscale SW directional coupler is proposed and studied by means of micromagnetic simulations and analytical theory. The interference between the two collective SW modes of two laterally parallel and dipolarly coupled magnetic waveguides separated by a gap provides a mechanism responsible for the operation of the device. The coupling length L, over which the energy of an SW is transferred from one waveguide to the other, is studied as a function of the SW wave number, geometry of the coupler, relative orientation of the static magnetization in the coupled waveguides, and the magnitude of the applied magnetic field (if it is used). The proposed design of the device allows one to use it as a directional coupler, as a controlled multiplexer, as a frequency separator, or as a power divider for microwave signals. Our micromagnetic simulations have also shown that the proposed device has an additional benefit: Its functionality can be dynamically reconfigured within tens of nanoseconds by application of a short pulse of an external bias magnetic field. Finally, the robustness of the coupler has been tested in additional numerical simulations, where geometric sizes were varied. These simulations ensured us that the experimental realization of the device is possible. The nanometer sizes of the proposed directional coupler and its ability to operate without external bias field make the proposed device interesting and useful for the processing of both digital and analog microwave signals at the nanoscale.

MATERIALS AND METHODS

Extraction of the dispersion relations from the results of micromagnetic simulation

The micromagnetic simulations were performed using the MuMax3 (*39*) code. It uses the Dormand-Prince method (*51*) for the integration of the LL-Gilbert equation

$$\frac{d\mathbf{M}}{dt} = -|\gamma|\mathbf{M}\times\mathbf{B}_{\text{eff}} + \frac{\alpha}{M_s}\left(\mathbf{M}\times\frac{d\mathbf{M}}{dt}\right) \quad (15)$$

where $\mathbf{M}$ is the magnetization vector; $\mathbf{B}_{\text{eff}}$ is the effective field that includes exchange, external, and demagnetization fields; γ is the gyromagnetic ratio; and α is the damping constant. The material parameters were given in the main text. There were three steps involved in the calculation of the SW dispersion curve in our simulation: (i) The external field was applied along the waveguide, and the magnetization was relaxed to a stationary state (ground state). This state was consequently used as the ground state in the following simulations. (ii) To excite odd and even SW width modes, a sinc field pulse was applied to a 20-nm-wide area located on one side of the waveguide. The sinc field is $b_y = b_0\text{sinc}(2\pi f_c t)$, with an oscillation field $b_0 = 1$ mT and a cutoff frequency $f_c = 20$ GHz. The $M_z(x, y, t)$ of each cell was collected over a period of $T = 100$ ns and recorded in $T_s = 25$-ps intervals, which allows a frequency resolution of $\Delta f = 1/T = 0.01$ GHz, whereas the highest resolvable frequency was $f_{\max} = 1/(2T_s) = 20$ GHz. The fluctuations in $m_z(x, y, t)$ were calculated for all the cells, $m_z(x, y, t) = M_z(x, y, t) - M_z(x, y, 0)$, where $M_z(x, y, 0)$ corresponds to the ground state obtained from the first step. (iii) To obtain the SW dispersion curves, we performed two-dimensional (2D) fast Fourier transformation (FFT) (*52*, *53*)

$$m_z(k_x, f) = \frac{1}{N}\sum_{i=1}^{N}\left|\mathcal{F}_2[m_z(x, y_i, t) - m_z(x, y_i, 0)]\right|^2 \quad (16)$$

where $\mathcal{F}_2$ is the 2D FFT, y_i is the ith cell along the width of the waveguide, and N is the total number of the cells along the width of the waveguide. To visualize the dispersion curve, we recorded a 3D color map of $P(k_x, f) \propto m_z(k_x, f)$ in logarithmic scale versus f and k_x, which is shown in Figs. 2 (E and F) and 4 (A and B). We performed 2D FFT on the time evolution and along the waveguide. Next, the average FFT amplitude was taken along the width of the waveguide. This method allows us to obtain information about all the SW modes (even and odd) existing in the waveguide.

SUPPLEMENTARY MATERIALS

Supplementary material for this article is available at http://advances.sciencemag.org/cgi/content/full/4/1/e1701517/DC1

movie S1. SW propagation in coupled waveguides.
movie S2. SW directional coupler acts as a multiplexer.
movie S3. Switching of the device functionality by changing the bias magnetic field.
movie S4. Ground-state switching: parallel to antiparallel.
movie S5. Ground-state switching: antiparallel to parallel.
movies S6 to S8. The effects of temperature on the directional coupler properties.

REFERENCES AND NOTES

1. V. V. Kruglyak, S. O. Demokritov, D. Grundler, Magnonics. *J. Phys. D Appl. Phys.* **43**, 264001 (2010).
2. A. Khitun, M. Bao, K. L. Wang, Magnonic logic circuits. *J. Phys. D Appl. Phys.* **43**, 264005 (2010).
3. D. E. Nikonov, I. A. Young, Overview of beyond-CMOS devices and a uniform methodology for their benchmarking. *Proc. IEEE* **101**, 2498–2533 (2013).
4. A. V. Chumak, A. A. Serga, B. Hillebrands, Magnonic crystals for data processing. *J. Phys. D Appl. Phys.* **50**, 244001 (2017).
5. M. Krawczyk, D. Grundler, Review and prospects of magnonic crystals and devices with reprogrammable band structure. *J. Phys. Condens. Matter* **26**, 123202 (2014).
6. A. V. Chumak, V. I. Vasyuchka, A. A. Serga, B. Hillebrands, Magnon spintronics. *Nat. Phys.* **11**, 453–461 (2015).
7. Y. Kajiwara, K. Harii, S. Takahashi, J. Ohe, K. Uchida, M. Mizuguchi, H. Umezawa, H. Kawai, K. Ando, K. Takanashi, S. Maekawa, E. Saitoh, Transmission of electrical signals by spin-wave interconversion in a magnetic insulator. *Nature* **464**, 262–266 (2010).
8. S. Urazhdin, V. E. Demidov, H. Ulrichs, T. Kendziorczyk, T. Kuhn, J. Leuthold, G. Wilde, S. O. Demokritov, Nanomagnonic devices based on the spin-transfer torque. *Nat. Nanotechnol.* **9**, 509–513 (2014).
9. K. Vogt, F. Y. Fradin, J. E. Pearson, T. Sebastian, S. D. Bader, B. Hillebrands, A. Hoffmann, H. Schultheiss, Realization of a spin-wave multiplexer. *Nat. Commun.* **5**, 3727 (2014).

10. P. Pirro, T. Brächer, A. V. Chumak, B. Lägel, C. Dubs, O. Surzhenko, P. Görnert, B. Leven, B. Hillebrands, Spin-wave excitation and propagation in microstructured waveguides of yttrium iron garnet/Pt bilayers. *Appl. Phys. Lett.* **104**, 012402 (2014).
11. V. E. Demidov, S. Urazhdin, R. Liu, B. Divinskiy, A. Telegin, S. O. Demokritov, Excitation of coherent propagating spin waves by pure spin currents. *Nat. Commun.* **7**, 10446 (2016).
12. A. Haldar, D. Kumar, A. O. Adeyeye, A reconfigurable waveguide for energy-efficient transmission and local manipulation of information in a nanomagnetic device. *Nat. Nanotechnol.* **11**, 437–443 (2016).
13. H. Yu, O. d'Allivy Kelly, V. Cros, R. Bernard, P. Bortolotti, A. Anane, F. Brandl, F. Heimbach, D. Grundler, Approaching soft x-ray wavelengths in nanomagnet-based microwave technology. *Nat. Commun.* **7**, 11255 (2016).
14. M. Collet, O. Gladii, M. Evelt, V. Bessonov, L. Soumah, P. Bortolotti, S. O. Demokritov, Y. Henry, V. Cros, M. Bailleul, V. E. Demidov, A. Anane, Spin-wave propagation in ultra-thin YIG based waveguides. *Appl. Phys. Lett.* **110**, 092408 (2017).
15. D. Bossini, S. Dal Conte, Y. Hashimoto, A. Secchi, R. V. Pisarev, Th. Rasing, G. Cerullo, A. V. Kimel, Macrospin dynamics in antiferromagnets triggered by sub-20 femtosecond injection of nanomagnons. *Nat. Commun.* **7**, 10645 (2016).
16. T. Schneider, A. A. Serga, B. Leven, B. Hillebrands, R. L. Stamps, M. P. Kostylev, Realization of spin-wave logic gates. *Appl. Phys. Lett.* **92**, 022505 (2008).
17. K.-S. Lee, S.-K. Kim, Conceptual design of spin wave logic gates based on a Mach-Zehnder-type spin wave interferometer for universal logic functions. *J. Appl. Phys.* **104**, 053909 (2008).
18. A. V. Chumak, A. A. Serga, B. Hillebrands, Magnon transistor for all-magnon data processing. *Nat. Commun.* **5**, 4700 (2014).
19. S. Klingler, P. Pirro, T. Brächer, B. Leven, B. Hillebrands, A. V. Chumak, Design of a spin-wave majority gate employing mode selection. *Appl. Phys. Lett.* **105**, 152410 (2014).
20. O. Zografos, B. Sorée, A. Vaysset, S. Cosemans, L. Amarù, P.-E. Gaillardon, G. D. Micheli, R. Lauwereins, S. Sayan, P. Raghavan, I. P. Radu, A. Thean, Design and benchmarking of hybrid CMOS-spin wave device circuits compared to 10nm CMOS, *IEEE Proceedings of the 15th International Conference on Nanotechnology*, Rome, Italy, 27 to 30 July 2015 (IEEE, 2016).
21. S. Klingler, P. Pirro, T. Brächer, B. Leven, B. Hillebrands, A. V. Chumak, Spin-wave logic devices based on isotropic forward volume magnetostatic waves. *Appl. Phys. Lett.* **106**, 212406 (2015).
22. S. Dutta, S.-C. Chang, N. Kani, D. E. Nikonov, S. Manipatruni, I. A. Young, A. Naeemi, Non-volatile clocked spin wave interconnect for beyond-CMOS nanomagnet pipelines. *Sci. Rep.* **5**, 9861 (2015).
23. A. A. Nikitin, A. B. Ustinov, A. A. Semenov, A. V. Chumak, A. A. Serga, V. I. Vasyuchka, E. Lähderanta, B. A. Kalinikos, B. Hillebrands, A spin-wave logic gate based on a width-modulated dynamic magnonic crystal. *Appl. Phys. Lett.* **106**, 102405 (2015).
24. K. Ganzhorn, S. Klingler, T. Wimmer, S. Geprägs, R. Gross, H. Huebl, S. T. B. Goennenwein, Magnon based logic in a multi-terminal YIG/Pt nanostructure. *Appl. Phys. Lett.* **109**, 022405 (2016).
25. N. Sato, K. Sekiguchi, Y. Nozaki, Electrical demonstration of spin-wave logic operation. *Appl. Phys. Express* **6**, 063001 (2013).
26. M. Balynsky, D. Gutierrez, H. Chiang, A. Kozhevnikov, G. Dudko, Y. Filimonov, A. A. Balandin, A. Khitun, A magnetometer based on a spin wave interferometer. *Sci. Rep.* **7**, 11539 (2017).
27. A. K. Ganguly, C. Vittoria, Magnetostatic wave propagation in double layers of magnetically anisotropic slabs. *J. Appl. Phys.* **45**, 4665–4667 (1974).
28. H. Sasaki, N. Mikoshiba, Directional coupling of magnetostatic surface waves in a layered structure of YIG films. *J. Appl. Phys.* **52**, 3546–3552 (1981).
29. A. V. Krasavin, A. V. Zayats, Active nanophotonic circuitry based on dielectric-loaded plasmonic waveguides. *Adv. Opt. Mater.* **3**, 1662–1690 (2015).
30. A. V. Sadovnikov, E. N. Beginin, S. E. Sheshukova, D. V. Romanenko, Y. P. Sharaevskii, S. A. Nikitov, Directional multimode coupler for planar magnonics: Side-coupled magnetic stripes. *Appl. Phys. Lett.* **107**, 202405 (2015).
31. A. V. Sadovnikov, E. N. Beginin, M. A. Morozova, Y. P. Sharaevskii, S. V. Grishin, S. E. Sheshukova, S. A. Nikitov, Nonlinear spin wave coupling in adjacent magnonic crystals. *Appl. Phys. Lett.* **109**, 042407 (2016).
32. A. V. Sadovnikov, A. A. Grachev, E. N. Beginin, S. E. Sheshukova, Y. P. Sharaevskii, S. A. Nikitov, Voltage-controlled spin-wave coupling in adjacent ferromagnetic-ferroelectric heterostructures. *Phys. Rev. Appl.* **7**, 014013 (2017).
33. T. Fischer, M. Kewenig, D. A. Bozhko, A. A. Serga, I. I. Syvorotka, F. Ciubotaru, C. Adelmann, B. Hillebrands, A. V. Chumak, Experimental prototype of a spin-wave majority gate. *Appl. Phys. Lett.* **110**, 152401 (2017).
34. K. Y. Guslienko, S. O. Demokritov, B. Hillebrands, A. N. Slavin, Effective dipolar boundary conditions for dynamic magnetization in thin magnetic stripes. *Phys. Rev. B* **66**, 132402 (2002).
35. K. Y. Guslienko, A. N. Slavin, Boundary conditions for magnetization in magnetic nanoelements. *Phys. Rev. B* **72**, 014463 (2005).
36. R. Verba, G. Melkov, V. Tiberkevich, A. Slavin, Collective spin-wave excitations in a two-dimensional array of coupled magnetic nanodots. *Phys. Rev. B* **85**, 014427 (2012).
37. R. V. Verba, Spin waves in arrays of magnetic nanodots with magnetodipolar coupling. *Ukr. J. Phys.* **58**, 758–768 (2013).
38. M. Beleggia, S. Tandon, Y. Zhu, M. De Graef, On the magnetostatic interactions between nanoparticles of arbitrary shape. *J. Magn. Magn. Mater.* **278**, 270–284 (2004).
39. A. Vansteenkiste, J. Leliaert, M. Dvornik, M. Helsen, F. Garcia-Sanchez, B. Van Waeyenberge, The design and verification of MuMax3. *AIP Adv.* **4**, 107133 (2014).
40. C. Dubs, O. Surzhenko, R. Linke, A. Danilewsky, U. Brückner, J. Dellith, Sub-micrometer yttrium iron garnet LPE films with low ferromagnetic resonance losses. *J. Phys. D Appl. Phys.* **50**, 204005 (2017).
41. H. Yu, O. d'Allivy Kelly, V. Cros, R. Bernard, P. Bortolotti, A. Anane, F. Brandl, R. Huber, I. Stasinopoulos, D. Grundler, Magnetic thin-film insulator with ultra-low spin wave damping for coherent nanomagnonics. *Sci. Rep.* **4**, 6848 (2014).
42. A. A. Serga, A. V. Chumak, B. Hillebrands, YIG magnonics. *J. Phys. D Appl. Phys.* **43**, 264002 (2010).
43. B. E. A. Saleh, M. C. Teich, *Fundamentals of Photonics* (John Wiley & Sons Inc., 1991).
44. Z. K. Wang, V. L. Zhang, H. S. Lim, S. C. Ng, M. H. Kuok, S. Jain, A. O. Adeyeye, Observation of frequency band gaps in a one-dimensional nanostructured magnonic crystal. *Appl. Phys. Lett.* **94**, 083112 (2009).
45. A. G. Gurevich, G. A. Melkov, *Magnetization Oscillations and Waves* (CRC Press, 1996).
46. R. Verba, G. Melkov, V. Tiberkevich, A. Slavin, Fast switching of ground state of a reconfigurable array of magnetic nano-dots. *Appl. Phys. Lett.* **100**, 192412 (2012).
47. R. Verba, V. Tiberkevich, K. Guslienko, G. Melkov, A. Slavin, Theory of ground-state switching in an array of magnetic nanodots by application of a short external magnetic field pulse. *Phys. Rev. B* **87**, 134419 (2013).
48. A. Haldar, A. O. Adeyeye, Deterministic control of magnetization dynamics in reconfigurable nanomagnetic networks for logic applications. *ACS Nano* **10**, 1690–1698 (2016).
49. M. Vogel, A. V. Chumak, E. H. Waller, T. Langer, V. I. Vasyuchka, B. Hillebrands, G. von Freymann, Optically reconfigurable magnetic materials. *Nat. Phys.* **11**, 487–491 (2015).
50. J. Gosciniak, S. I. Bozhevolnyi, T. B. Andersen, V. S. Volkov, J. Kjelstrup-Hansen, L. Markey, A. Dereux, Thermo-optic control of dielectric-loaded plasmonic waveguide components. *Opt. Express* **18**, 1207–1216 (2010).
51. J. R. Dormand, P. J. Prince, A family of embedded Runge-Kutta formulae. *J. Comput. Appl. Math.* **6**, 19–26 (1980).
52. D. Kumar, O. Dmytriiev, S. Ponraj, A. Barman, Numerical calculation of spin wave dispersions in magnetic nanostructures. *J. Phys. D Appl. Phys.* **45**, 015001 (2012).
53. G. Venkat, D. Kumar, M. Franchin, O. Dmytriiev, M. Mruczkiewicz, H. Fangohr, A. Barman, M. Krawczyk, A. Prabhakar, Proposal of a standard micromagnetic problem: Spin wave dispersion in a magnonic waveguide. *IEEE Trans. Magn.* **49**, 524–529 (2013).

Acknowledgments

Funding: This research was supported by the European Research Council Starting Grant 678309 MagnonCircuits. R.V. acknowledges support from the Ministry of Education and Sciences of Ukraine (project 0115U002716). A.S. was supported by grants ECCS-1305586 and EFMA-1641989 from the U.S. NSF, by a contract from the U.S. Army TARDEC (Tank Automotive Research, Development and Engineering Center) and RDECOM (Research, Development and Engineering Command), and by the Center for NanoFerroic Devices (CNFD) and the Nanoelectronics Research Initiative (NRI). **Author contributions:** Q.W. proposed the spin-wave directional coupler design, performed micromagnetic simulation, and wrote the first version of the manuscript. P.P. and A.V.C. devised and planned the project. R.V. and A.S. developed the general analytical theoretical model. A.V.C. led the project. All authors discussed the results and contributed to writing the manuscript. **Competing interests:** The authors declare that they have no competing interests. **Data and materials availability:** All data needed to evaluate the conclusions in the paper are present in the paper and/or the Supplementary Materials. Additional data related to this paper may be requested from the authors.

Submitted 9 May 2017
Accepted 14 December 2017
Published 19 January 2018
10.1126/sciadv.1701517

Citation: Q. Wang, P. Pirro, R. Verba, A. Slavin, B. Hillebrands, A. V. Chumak, Reconfigurable nanoscale spin-wave directional coupler. *Sci. Adv.* **4**, e1701517 (2018).

Reconfigurable nanoscale spin-wave directional coupler

Qi Wang, Philipp Pirro, Roman Verba, Andrei Slavin, Burkard Hillebrands and Andrii V. Chumak

Sci Adv **4** (1), e1701517.
DOI: 10.1126/sciadv.1701517